Materials & Design 244 (2024) 113218

Contents lists available at ScienceDirect

Materials & Design

journal homepage: www.elsevier.com/locate/matdes

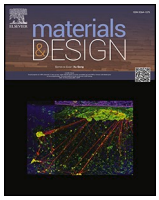

Subcutaneous coding via laser directed energy deposition (DED-LB) for unalterable component identification

Aizpea Urresti [1], Jon Iñaki Arrizubieta [*,2], Aitzol Lamikiz [3], Ibon Holgado [4], Naiara Ortega [5]

Department of Mechanical Engineering, University of the Basque Country (UPV/EHU), Plaza Torres Quevedo 1, Bilbao 48013, Spain

ARTICLE INFO

Keywords:
Subcutaneous
Coding
Identification
DotCode
Additive manufacturing
Laser directed energy deposition
Unalterable

ABSTRACT

Part identification has become a priority in manufacturing, especially when it comes to the additive manufacturing (AM) industry, where the counterfeit printing of almost any digitalized component is possible. As a means of avoiding forgery, the development of non-detectable labels, or digital passports is necessary. In the present work, a novel methodology for printing subcutaneous coding on aeronautical parts is proposed thanks to the multimaterial capabilities of the laser based directed energy deposition (DED-LB). The coding is based on embedding a dot pattern of a high-density alloy on a small area of a lower density component, which once covered and finished generates a pattern only visible by X-ray imagining. The viability of the proposed methodology is proven by embedding WC particles on a Ti6Al4V substrate. Firstly, the most relevant process parameters are optimized to ensure a sharp and a readable code, and their geometry is analysed by means of industrial Computed Tomography (CT). Also, the metallurgical quality and chemical composition of the generated dots is evaluated by Scanning Electron Microscope (SEM). Finally, a demonstrator part is fabricated with a hidden code. The code readability and the mechanical properties are tested to ensure the feasibility of the developed methodology.

1. Introduction

In a modern world where companies are in a constant fight to develop and protect their knowledge and products, forgery has become a major challenge to an innovation-driven global economy. According to Europol counterfeited and pirated products represent the 5 % of the total imports of the EU [1]. Such products range from high-end consumer luxury goods such as watches, to business products including machines, chemicals, or spare parts.

In order to avoid these problems, component marking has been widely employed [2], where direct and indirect strategies are differentiated. Nevertheless, to prevent counterfeiting direct methods such as dot peening, electrolytic chemical etching, engraving, etc. are required. In this area, Velotti et al. explored the capabilities of laser marking for ensuring the identification and traceability of titanium components for aerospace applications [3]. Going one step ahead, Ludasi et al. studied the laser ablation of medical components packaging to ensure their traceability and reduce counterfeiting issues [4]. Also, Teutoburg-Weiss et al. studied the capabilities of laser texturing for complex pattern manufacturing [5]. However, the main limitation of the above-mentioned coding systems is that the code is situated on the surface. Consequently, it can result damaged during the lifespan of the component and is vulnerable to piracy as it is visible and therefore, replicable.

Another well-explored alternative is the use of fluorescence, which is one of the most widely employed anti-counterfeiting technologies [6]. Unfortunately, applying this alternative to metallic components is not viable, unless indirect marking methods are employed and they present the disadvantage of being detachable, and therefore, forgeable. Alternatively, Speidel et al proposed the electrochemical etching of unique dendritic marks as a means of visual identification of metallic parts [7].

* Corresponding author.
E-mail addresses: aizpea.urresti@ehu.eus (A. Urresti), joninaki.arrizubieta@ehu.eus (J.I. Arrizubieta), aitzol.lamikiz@ehu.eus (A. Lamikiz), ibon.holgado@ehu.eus (I. Holgado), naiara.ortega@ehu.eus (N. Ortega).
[1] Orcid: https://orcid.org/0000-0002-1768-8206
[2] Orcid: https://orcid.org/0000-0002-6030-4941
[3] Orcid: https://orcid.org/0000-0002-8477-0699
[4] Orcid: https://orcid.org/0000-0003-1723-7373
[5] Orcid: https://orcid.org/0000-0001-8283-847X

https://doi.org/10.1016/j.matdes.2024.113218
Received 19 April 2024; Received in revised form 12 July 2024; Accepted 29 July 2024
Available online 2 August 2024

But as they are positioned on the surface, they are alterable, and they can result damaged during the service life of the component.

One of the factors that facilitates the counterfeiting of industrial components is the development of additive manufacturing (AM), since it allows the direct printing of any digitized component. Counterfeiters with AM machines and the corresponding CAD models, which can be downloaded from the internet or acquired through reverse engineering, can easily copy the desired products. Actually, as AM is based on printing components from a CAD file, anyone with the CAD file can print the part. In this direction, Chen et al. developed a method for embedding security defective-design-features into the CAD files [8]. Consequently, unless precise printing parameters are used, the manufacturing results in defective or inferior quality components. Similar methods have been developed by Raeker-Jordan et al. [9]. Nevertheless, these methods do not allow identifying already existing components, as no internal identifying systems were embedded within the AM manufactured part.

The same AM process that is being used for component forgery can be used to fight counterfeiting. For instance, Maia et al. presented a LayerCode strategy for printing polymeric components that are readable with any conventional camera [10]. However, surface coding techniques such as laser marking or printing barcodes visible from the outside are easily detectable and susceptible to forgery, so hidden coding strategies are required in strategic components or sectors. Unfortunately, manufacturing internal features is a complex task, even more when referred to metallic parts. The technical limitations of existing metal AM technologies, including laser-based powder bed fusion (PBF-LB) and laser-based directed energy deposition (DED-LB), make difficult embedding high resolution security features [11].

Research has been done in this field and the first attempts to embed physical tags, such as barcodes or QR codes, within manufactured components that work as permanent and unique identifiers have been published. Chen et al. developed an image analysis method for obtaining accurate and legible internal QR codes based on PBF-LB [12]. They employed a single material and printed the codes as void regions, which were revealed through computed tomography (CT). However, the powder from the inside of the QR code cannot be eliminated, what reduces the code resolution, and affects the mechanical properties of the resulting part. Likewise, Eisenbarth et al. proposed to intentionally generate internal inhomogeneities during the PBF-LB to create patterns that are then identified with eddy currents [13]. Nevertheless, these voids and lack of fusion defects could promote crack initiation and their influence on the behaviour of the component was not studied.

Wei et al. applied a hybrid powder delivery system for PBF-LB to embed safety features of dissimilar labelling materials into metallic components [11]. They analysed the viability of infrared thermography, X-ray imaging, and X-ray fluorescence. They concluded that the X-ray imaging is the most promising technique, capable of identifying embedded features up to 15 mm in depth for the studied materials, AISI 316l and Cu10Sn. Nevertheless, the similar density of the materials employed in the research, limits the readability of the embedded information. Besides, the PBF-LB technology is not adequate for multimaterial processes, and its industrialization would be a complex task.

Additive friction stir deposition (AFSD) has also been employed for embedding QR codes [14]. The QR code was laser micromachined to produce features of approximately 15 μm deep and then, it was coated via AFSD. CT was employed for code visualization, what enabled reading codes situated relatively far from the surface. However, this AM method was only valid for low melting point metal alloys, such as aluminium.

On the contrary, the powder-based DED-LB is an additive process capable of combining various materials and even create in situ mixtures [15], which offers a high flexibility in the component design [16]. Salas et al. proved the capability of DED-LB for creating multimaterial components with a variable magnetic response [17]. Nevertheless, the resolution of the measurement depends on the code depth and low readability was obtained at high depths. Eisenbarth et al. also proposed to embed codes through parameter variation in DED-LB, what led to coatings of varying depth that can be detected afterward via eddy currents [13]. However, accurate code readings were only possible when they were positioned close to the surface. Besides, this method was only valid when a wrought component is coated by a single DED-LB layer, and not for including a code in an AM printed part or when multilayer coatings are required.

Overall, due to the complexity of the problem and the differences in part materials and methods, no standard has been set. On the one hand, laser marking or etching strategies for product coding create visible labels situated at the surface and therefore, they can be altered or damaged during the service life of the components. On the other hand, codes based on modifying the internal structure of the components, such as inducing defects that can be detected via eddy currents or varying the magnetic behaviour through combining different materials, enable a low-cost code reading. Nevertheless, the code needs to be situated close to the surface to ensure readability. This can affect the component behaviour, especially when it comes to surface hardness, wear resistance, biocompatibility and osteointegrability of the original part, which is of utmost importance for medical or aeronautical sectors. Finally, embedded code detection through X-ray and CT has been proven to be effective. Codes situated at higher depths can be read accurately, but the material combination and manufacturing procedure is critical to ensure a clear and readable code, which has yet to be resolved.

In view of the necessity of creating undetectable marking strategies to tackle counterfeiting, a novel coding system is developed based on the multimaterial capabilities of the DED-LB process. In the present work a high-density alloy is embedded in a low-density alloy to generate an internal DotCode which is undetectable, unalterable, and only visible by penetrating techniques such as X-ray inspection. This coding system is selected for the validation of the methodology, because it consists of individual dots, where no high geometrical resolution is required, which makes it appropriate for its manufacturing via DED-LB. A combination of Ti6Al4V grade Titanium base and tungsten carbide (WC) inclusions is chosen, based on the wide use of Titanium for aeronautical and medical applications [18], and the elevated density of WC, which is 3.5 times that of the base material. The compatibility of this material combination for metal matrix composite (MMC) manufacturing by DED-LB has already been proven by Yang et al. [19], and a subsequent study presented by Oyelola et al. tested its machinability and mechanical properties, concluding that the WC inclusions do not cause cracking or act as failure initiation points [20]. Nevertheless, in the present work a DotCode example is printed and the resulting mechanical properties in the coded components are evaluated to prove the validity of the developed coding system.

2. Methodology

2.1. Experimental tests

The objective of printing subcutaneous codes for component identification is a complex task, and therefore, it is planned according to the following methodology, see Fig. 1(a). In a first step, the process parameters were optimized through single pulse tests for ensuring detectable, defect-free dots, and in a second step, a real DotCode was printed and validated on a titanium plate.

For single dot characterization, step 1, and the code printing, step 2, 90x51x10 mm^3 titanium slabs were employed as substrates. The tungsten carbide (WC) powder was provided by Oerlikon Metco (Metcoclad 52001) and Ti6Al4V powder manufactured by Carpenter was employed for hiding the printed DotCode. The particle size of both powders was in the range of 45 to 106 μm and they had been manufactured via inert gas atomization, which ensured the spherical shape of the particles.

A 5-axis laser processing unit with a 1 kW fibre laser from Coherent was used for the experimental tests. The powder material was delivered by a Metco Twin 10-C Sultzer feeder, employing 99.99 % purity Argon

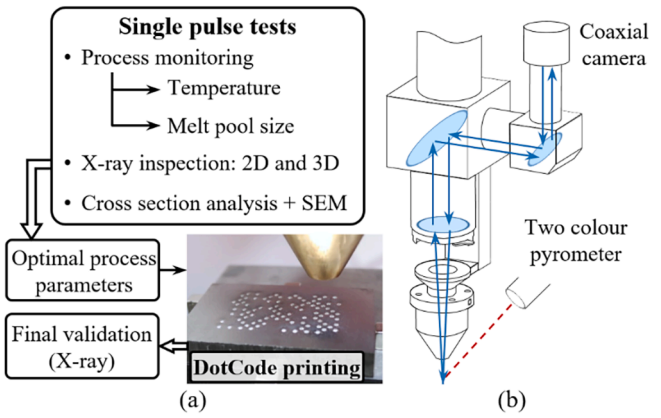

Fig. 1. Schematic diagrams of the process methodology. (a) Single pulse optimization and DotCode printing process. (b) Monitoring setup employed during single pulse tests.

for the carrier and shielding gas, which were set to 5 $l \cdot min^{-1}$ and 15 $l \cdot min^{-1}$, respectively. A coaxial continuous nozzle was employed, and the work plane was located 15 mm below its tip.

For the optimum parameter definition a 45 single pulse design of experiments (DOE) was performed varying the laser power (P=400, 500, and 600 W), the pulse duration (t = 0.1, 0.2, and 0.3 s), and powder mass rate (Q=1, 2, 3, 4, and 5 $g \cdot min^{-1}$). The characteristics of all the performed tests are detailed in Appendix 1. During the dot fabrication, the melt pool size and maximum temperature were monitored through a coaxial camera and a two-colour pyrometer (Fig. 1(b)), respectively. A CS135MUN NIR-camera from Thorlabs with an acquisition frequency of 160 Hz was employed to capture the melt pool geometry. The maximum temperature of the melt pool was measured by an IGAR 12-LO two-colour pyrometer, which has a 549–2500 °C measuring range and a 150 Hz acquisition frequency.

2.2. X-ray imaging and sample analysis

The readability of the single pulse and the final DotCode were tested by X-ray imaging. For this purpose, the X-Cube compact 225 from General Electric was used, Fig. 2(a). Expanded polystyrene was used to clamp and elevate the samples from the 3-jaw chuck, as shown in Fig. 2 (b), both in the case of X-ray imaging and Computed Tomography (CT). The maximum voltage and current of the CT system were 195 kV and 2.8 mA, respectively. The focus size was 0.4 mm, and the resulting voxel size was 94.856 μm. The beam hardening reduction was performed through the combination of 1 mm copper and 0.5 mm tin filters.

The 2D images obtained by X-ray were post processed by a grayscale transformation by adjusting the white to the base titanium material and the black to the fabricated WC points. In order to test the readability of each dot, the black threshold was set so that only the darkest pixels turn fully black. Fig. 3 shows the raw X-ray image and the enhanced image. It must be noted that the readability of all dots could be improved by increasing the contrast further during the post processing. However, a more restrictive approach was adapted to obtain suitable parameters for more extreme conditions, such as larger parts.

Moreover, the geometries of single pulse dots were also analysed by CT, and for this purpose cylindrical samples were extracted through wire electrical discharge machining (w-EDM) around the selected pulses. All cylindrical samples were scanned under the same conditions and orientations into the machine. The obtained data was processed using VGStudio MAX 3.4 software and the volume of the high-density regions was calculated after surface segmentation. For this purpose, the Advanced Surface Determination tool, whose morphological operations are shown in Fig. 4, was employed starting from a specified point on the CT histogram. The selection was expanded as long as neighbouring voxels maintained grey values within the designated tolerance range of 3000 grey number units. Finally, the local adaptive thresholding algorithm was reapplied to the surface obtained in the previous step.

Finally, cross sections of the single pulse tests were cut through w-EDM and they were analysed under an optical and a scanning electron microscope (SEM). All samples were ground and polished following an appropriate metallographic procedure, to avoid pulling out the WC particles from the Ti6Al4V matrix, which may damage the sample. In addition, those prepared for metallographic analysis under the Leica DCM-3D microscope were etched by Kroll's reagent. Finally, a compositional analysis of the deposited layers was performed by means

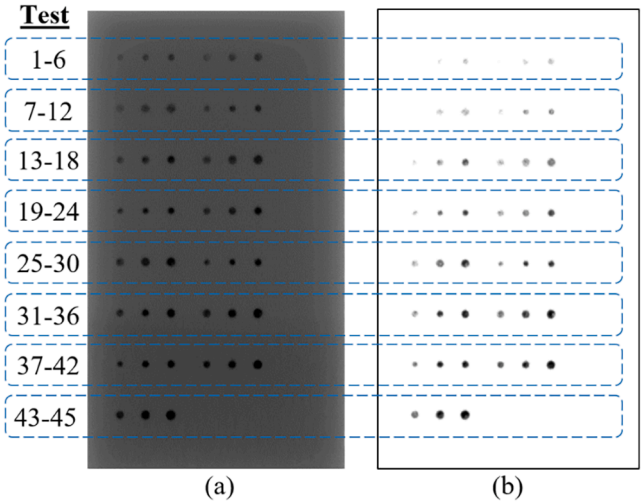

Fig. 3. X-ray images of the 45 single pulse tests. (a) Raw X-ray image. (b) High contrast image treated in Matlab for single pulse readability analysis.

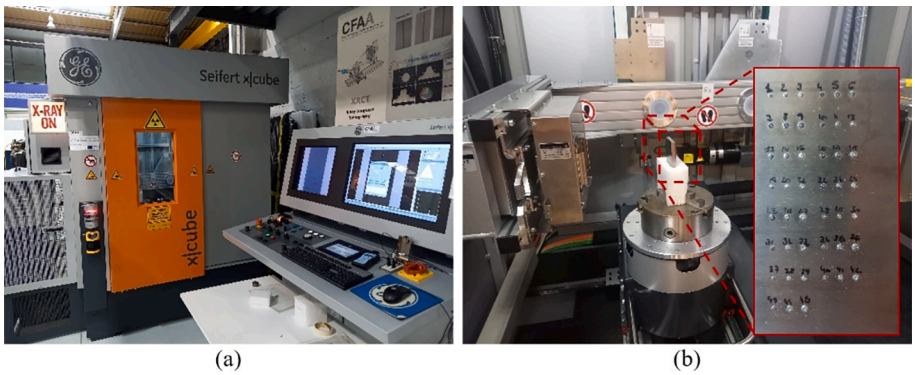

Fig. 2. Set-up for X-ray inspection and Computed Tomography. (a) X-Cube machine. (b) Positioning of the single pulse test part.

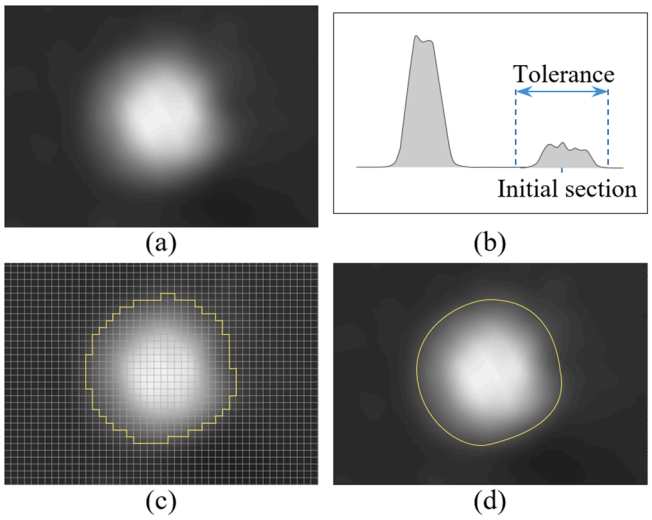

Fig. 4. Morphological operations for the dot region segmentation. (a) Original volume. (b) Expansion of the initial high-density section based on tolerance value. (c) Extended selection. (d) Final selection after local adaptive thresholding.

of scanning electron microscopy (SEM) and energy-dispersive X-ray spectroscopy (EDS) microanalysis equipment (Tescan Vega Compact). Discrete compositional measurements were performed at the different samples manufactured in the single pulse tests and the chemical composition of the material was obtained.

2.3. Demonstrator part manufacturing

After obtaining suitable parameters for code printing, a demonstrator part was manufactured to test the viability to produce X-ray readable codes on an embedded specimen. The code designed for the purpose of this research was the word "certified" which created the pattern shown in Fig. 5(a) according to the *ISS DotCode Symbology Specification 4.0* standardised by the Association for Automatic Identification and Mobility (AIM). Based on the dot diameter of the chosen parameter set, a spacing of 3 mm was set between diagonally located dots. The result was a 43x30 mm^2 code which was printed on a 90x51x10 mm^3 substrate, and coated by two layers of Ti6Al4V with a height of 0.8 mm each, as seen on Fig. 5(b). Later, the plate was ground by 0.4 mm to eliminate any signs of DED-LB processing.

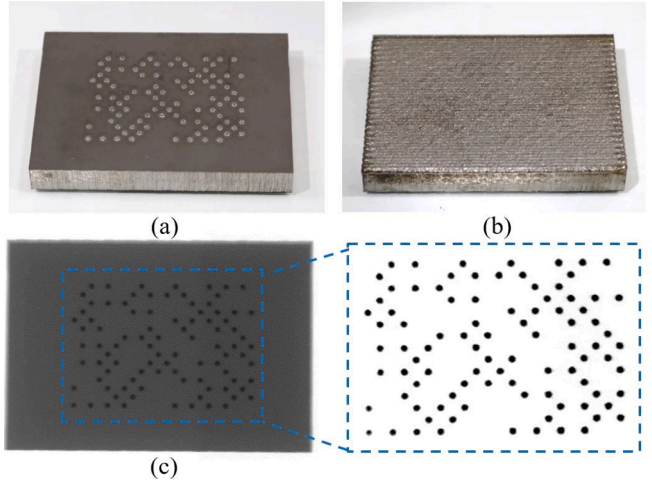

Fig. 5. DotCode manufacturing and X-ray validation process. (a) DotCode printing. (b) Code embedding by Ti6Al4V layers. (c) X-ray imaging and code validation.

The final specimen was inspected by X-ray imaging from both sides to test the depth independence of the readability of the code. The code area was cropped and treated in the same manner to the single pulses, and the resulting image was validated by computer programming, Fig. 5 (c).

2.4. Mechanical property tests

The effect of the proposed methodology on the mechanical properties of the base material was studied by means of 3-point bending tests and Rockwell hardness tests. The 3-point bending tests were performed on an INSTRON 8801 testing machine with a cross-head speed of 1 $mm{\cdot}min^{-1}$ and a 100 kN load cell. Fig. 6 shows the schematic description of the testing setup and sample types.

Nine samples of three different types were extracted from the demonstrator part, comprising the base Ti6Al4V material, the base Ti6Al4V material with a DED-LB deposited coating of the same material, and the base Ti6Al4V material in which a WC code is embedded and covered with a DED-LB deposited coating, whose cross sections are shown in Fig. 6(b), Fig. 6(c), and Fig. 6(d) respectively.

The Rockwell hardness measurements were taken on an ERNST Computest SC machine, which employed a 11.8 N preload and a 49 N testing load. Ten hardness measurements were performed on the base material and the coded surfaces.

3. Results and discussion

3.1. Single pulse test monitoring

The melt pool temperature extracted from Tests 1 through 9, which corresponded to the lowest WC powder feed rate value, is shown in Fig. 7. As it can be clearly seen, the melt pool was created almost instantaneously in all tests, and the maximum temperature reached increased when rising the employed laser power. Moreover, the cooling rate was also almost invariable for the different laser powers and WC mass rates, despite showing a small reduction when increasing laser power. Therefore, it was concluded that for a certain laser power and

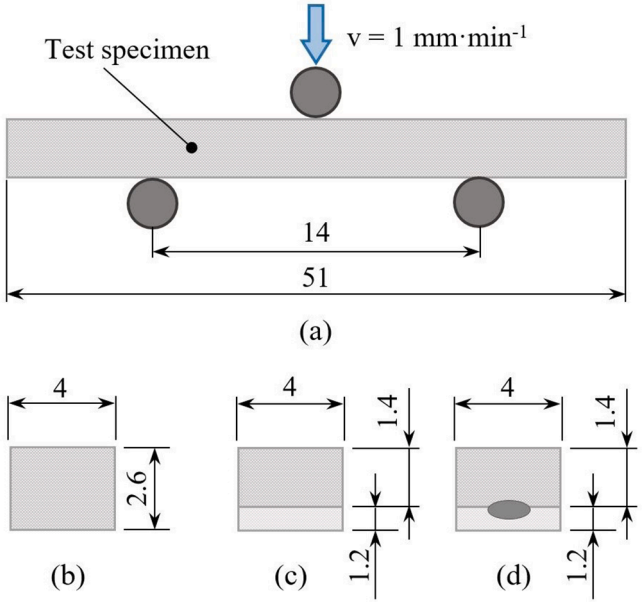

Fig. 6. Schematic description of 3-point bending tests setup and sample types. a) Test setup, b) Ti6Al4V base material, c) Ti6Al4V base and Ti6Al4V coating, and d) Ti6Al4V base with WC dots and Ti6Al4V coating. All distance units are in millimetres.

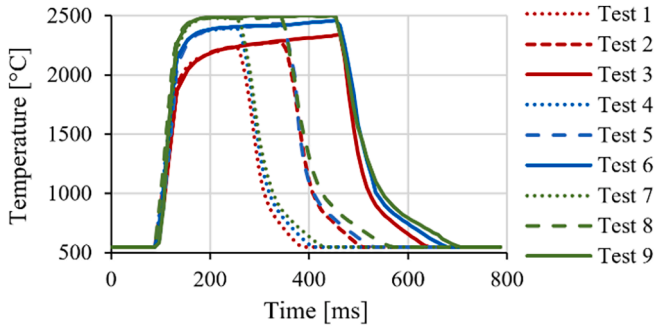

Fig. 7. Melt pool maximum temperatures measured by the coaxial pyrometer. Line colour indicates laser power (P) red = 400 W, blue = 500 W and green = 600 W, and line type indicates pulse duration (t) dots = 0.1 s, dashes = 0.2 s and solid lines = 0.3 s.

powder mass rate, the amount of WC introduced into the melt pool is linearly proportional to the pulse duration. However, the exact number of particles cannot be predicted, as it follows a stochastical distribution where the power feeder ensures an almost constant mass flow, but the amount of powder particles varies depending on their diameter.

The optical measurements of the dots upper surfaces obtained from this inspection are detailed in Appendix I, and have led to the conclusion that the rise in laser power had the most impact on the increase of the dot diameter, followed by the laser pulse duration. Regarding the metallurgical integrity, no visible cracks were observed at this stage, which is necessary if the codified components are to be fully functional.

3.2. Single pulse test X-ray imagining analysis

The optimal pulse fabrication parameters were chosen based on the intensity profiles of each dot. Ideally, a top hat profile is desired for the optimal dot intensity as it maximises the readability of the code. After applying the described grayscale transformation, Tests 39 and 45 were identified as the optimal parameter sets (Table 1). The results for the Test 9 parameter set have also been included on the following analysis, in order to compare the maximum resolution results with a low contrast counterpart.

The reason for choosing two optimal parameter sets lays in their geometry. As seen in Fig. 8, Test 39 was fabricated employing the lowest power value (P=400 W) and offered a small but sharp-edged pulse, which increased the spatial resolution of the code. Meanwhile, the Test 45 employed the highest powder value (P=600 W), which offered maximum saturation and increased readability, at the cost of a larger dot size.

Their X-ray intensity profiles are shown on Fig. 8, alongside their microscopic surface and coaxial camera images. It was generally observed that higher values of pulse duration resulted in better X-ray readability, but nonetheless, powder mass rate values over 4 $g{\cdot}min^{-1}$ were necessary to obtain sufficiently readable dots. The coaxial camera images of Fig. 8 illustrate the increase of WC particles being injected in the melt pool at the 0.2 s pulse instant, as well as an increase of the melt pool size between tests 39 (Fig. 8(b)) and 45 (Fig. 8(c)). The improved readability of the optimized parameter sets can also be observed by comparing the optical and X-ray measurements of the dot diameter, and the respective deviation in Fig. 8.

Table 1
Single pulse results, where P is the laser power, t the pulse duration and, Q the WC mass rate.

No.	P (W)	t (s)	Q (g/min)	Measured diam. (mm)	CT diam. (mm)	Deviation (%)
9	600	0.3	1	2.140	1.353	36.78
39	400	0.3	5	1.595	1.576	1.21
45	600	0.3	5	2.055	2.013	2.06

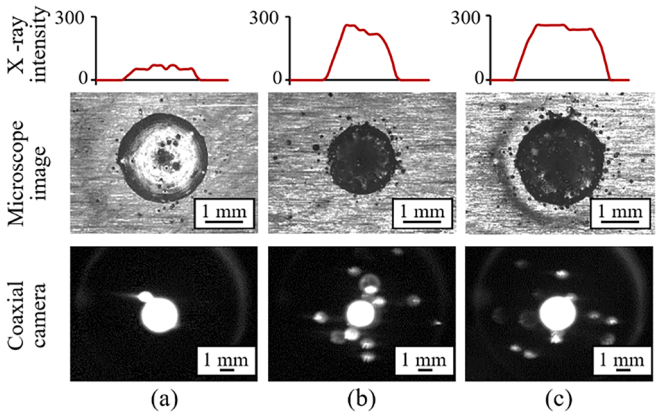

Fig. 8. X-ray intensity diagram, microscope surface image, and coaxial camera frame at t = 0.2 s pulse instant. (a) Low contrast reference parameter set test 9. (b) Optimal parameter set for high spatial resolution test 39. (c) Optimal parameter set for high X-ray resolution test 45.

Overall, the X-ray results demonstrate that WC mass rate was the parameter most closely related to the X-ray readability, followed by pulse duration. The optimal values of these parameters resulted in dots of suitable readability regardless of the employed laser power value, it was possible to identify two optimal parameter sets for different purposes according to the part geometry: Test 39 parameters for increased spatial resolution and Test 45 parameters for increased readability.

3.3. Cross section analysis

Fig. 9 shows the cross-section images of Tests, 9, 39, and 45. From these images it can be seen that the metallurgical integrity of the substrate material was maintained in all cases, and no cracking occurred as

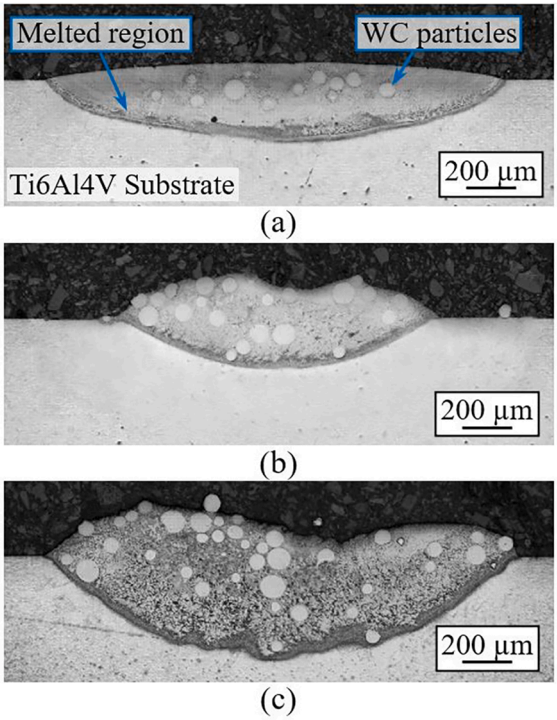

Fig. 9. Single dot cross sections obtained in an optical microscope. (a) Low contrast reference parameter set test 9. (b) Optimal parameter set for high spatial resolution test 39. (c) Optimal parameter set for high X-ray resolution test 45.

a result of embrittlement of the metallic matrix by WC inclusions. Moreover, no lack of fusion or gas porosity defects were detected during the analysis. These results support the hypothesis that the code printing will not act as crack initiators on an in-service part and are in accordance with those obtained on [19] and [20].

Concerning WC particle injection, Fig. 9 shows a significantly lower number of particles in the samples corresponding to Test 9 (Fig. 9(a)) in comparison to Tests 39 and 45 (Fig. 9(b) and (c)). These cross-section images also show that the distribution of particles within the melt pool was not homogeneous, as Tests 39 and 45 present a higher concentration in the left side of the dot. This heterogeneity explains the peaks on the intensity profiles in Fig. 8. However, as proved by the readability analysis, this phenomenon does not hinder the X-ray readability of the dot. These cross sections were further studied by means of SEM and EDS, with the aim of analysing the metallurgical properties of the Ti6Al4V matrix microstructure as a result of the WC particle inclusions.

The secondary electron SEM images on Fig. 10 show a good metallurgical bond between particle and substrate. The use of the secondary electrons make the phases with the heaviest components bright white and the lightests ones black. In the case of Fig. 10(a) the heaviest elements are the WC powder particles, and the lightest one corresponds the encapsulating resin, followed by the titanium substrate. A larger magnification image of the centre of the dot is shown on Fig. 10(b), in order to locate the central and lower regions of the dot.

The region shown on Fig. 10(d) corresponds to the bottom of the melted material. The lack of brightness on the lower end indicates that the W content decreases on the areas closer to the melt pool boundary, where the melted substrate material had an upwards movement due to the buoyancy force. This movement of material suggests that a longer pulse duration time might not be correlated with a higher W content on the matrix, as the Ti content of the matrix will also increase as the substrate material enters the melt pool.

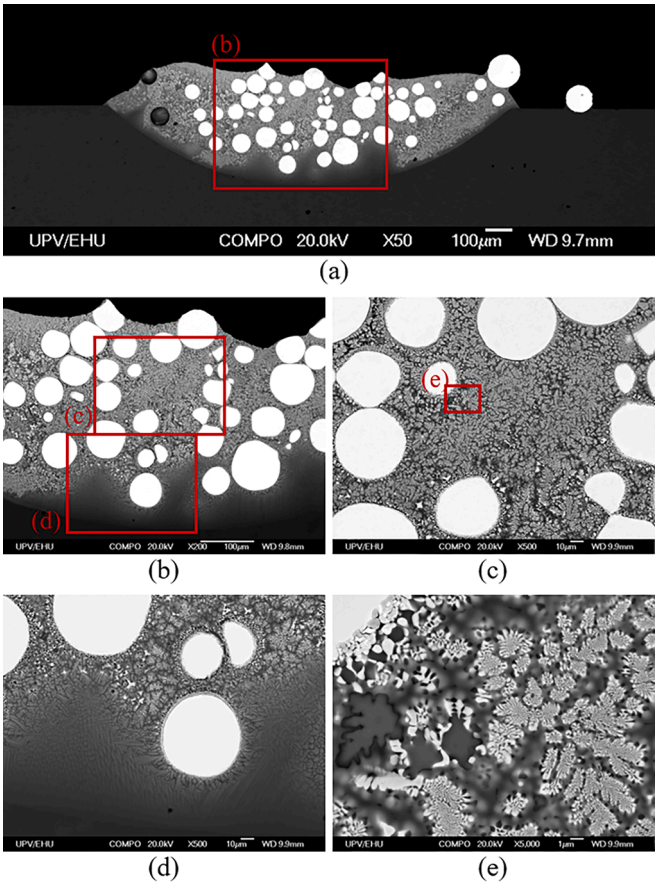

Fig. 10. Secondary electron SEM images of the microstructure on Test 39. (a) Test 39 cross section, (b) Test 39 central detail at x200 magnification, (c) Test 39 central detail at x500 magnification, (d) Test 39 lower end detail at x500 magnification and (e) Test 39 microstructure near WC particle at x5,000 magnification.

The microstructure on the centre of the dot is shown on Fig. 10(c), where it is is once again proven that no cracking is present were high concentration of WC particles occurs. Fig. 10(e) shows a detailed image of the microstructure around a WC particle. The matrix microstructure on Fig. 10(e) shows an initial dissolution of the WC particle near its surface, followed by the formation of an dendrite-like structure. Discrete compositional measurements in the phases near a single WC particle for the Tests 9 and 39 are shown on Fig. 11.

The analysis results confirmed that Tungsten (W) precipitation was mostly concentrated on the leaf-like phases of the matrix (brightest phases), which is why these are referred as W enriched phases. Although the W content in these phases decreased in the measurements further away from the WC particles (both from 9D to 9E or from 39A to 39B), when comparing the measurements for the W enriched phases in Test 9 and Test 39, it was observed that the overall content of W was significantly higher in the latter as a consequence of the higher WC mass rate. Consequently, this also increased the W content of the whole dot, and hence, the resulting density of the MMC. The previous compositional tendencies were also seen in the Titanium enriched phases (dark phases), which in the case of the Test 39 (39E, 39D, 39F) presented a W content that doubled that of Test 9 (9F, 9G).

A more general analysis of the microstructure of the matrix further away from the particles (Fig. 12(a)) revealed microstructural changes between the upper and central region of the dot, as shown on the magnified image on Fig. 12(b). The microstructure on the upper region of the dot showed a fine, leaf-like morphology, which is illustrated on Fig. 12(c), where the Titanium enriched matrix formed vein-like structures around the W enriched phase. Additionally, dark precipitates were identified on the periphery of the W enriched phase. Fig. 12(d) shows the microstructure formed on the centre of the dot, where the W enriched phase was coarser and more homogeneously dispersed due to its circular geometry. In this case, the precipitates were also present.

Due to the location of each microstructure type on the dot cross section, it is concluded that the microstructural change is related to the cooling rate of the material. The upper region of the melt pool cools faster than the central region due to the convection of the protective Argon gas flow, which results on a finer microstructure. Meanwhile, in the centre region of the dot, heat is only released through conduction, resulting on a slower solidification and coarser microstructure.

The EDS compositional maps of the fine and coarse microstructures are shown on Fig. 12(e) and Fig. 12(f), respectively. In both cases, the brightest phases were confirmed to be mainly composed of W and C, while the matrix was primarily composed by Ti, with Al, W, and C also being present. Although Al was to be expected as the metallic matrix is Ti6Al4V, the presence of W and C further proved the diffusion of these elements onto the matrix, supporting the previous statement that density of the whole dot is increased as a result of the MMC. Moreover, the precipitates were identified as TiC, which nucleated preferentially around the W enriched phase surface.

These compositional results demonstrate that the generated dot has a higher density not only in the individual locations of the discrete WC particles, but also in the whole region melted by the laser. As a result, it is proven that the X-ray intensity of the fabricated dots does not depend on the distribution of particles within it, but rather, the number of particles injected and the concentration of W in the matrix.

3.4. Single dot CT analysis

The X-ray detection capability of the optimal pulses (Tests 39 and 45) was tested alongside reference low contrast parameter set (Test 9). The

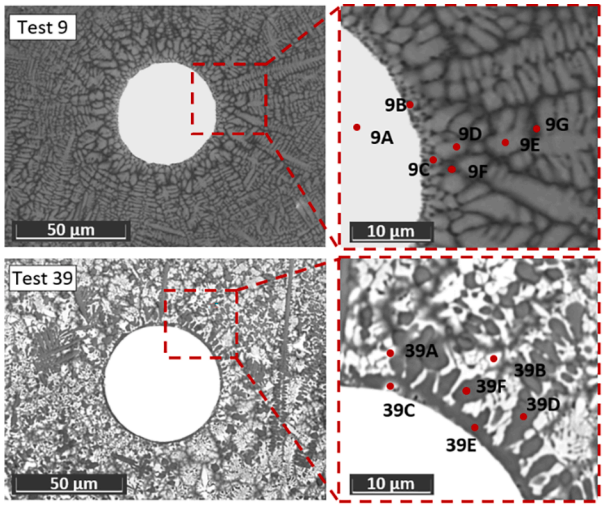

Point	W	Ti	C	Al	V
9A	86.22		13.78		
9B	42.74	44.01	9.36	1.82	2.07
9C	29.97	57.24	7.09	3.00	2.70
9D	29.82	57.67	6.81	3.03	2.67
9E	27.89	60.49	5.84	3.01	2.78
9F	11.60	74.96	6.46	3.80	3.19
9G	7.92	77.94	7.68	3.27	3.19
39A	80.32	8.80	9.50	0.39	0.98
39B	79.74	8.47	10.45	0.37	0.98
39C	41.34	42.36	14.86	0.04	1.41
39D	26.92	56.23	15.38	0.01	1.46
39E	24.97	57.75	15.60	0.28	1.40
39F	24.81	59.41	13.96	0.32	1.50

Fig. 11. Scanning Electron Microscopy images and their respective discrete chemical composition measurements (%). Low contrast reference parameter set test 9 and, high spatial resolution optimal parameter set test 39.

analysed cylindrical samples had a 6 mm diameter resulting on a voxel size of 94.856 µm and considering the WC particle diameter range is between 45 and 106 µm, the detection of individual particles by CT was not possible. Instead, the employed software allowed the measurement of a high-density area, represented by the lighter coloured pixels in comparison to the darker substrate.

Fig. 13 shows the 3D image and corresponding segmented volume for each pulse. These results confirm that the pulses fabricated using the optimal parameters (Tests 39 and 45) allowed a much better detection than the low contrast dot (Test 9) chosen for reference. Furthermore, the increased density of the dot matrix was also proved by CT.

3.5. DotCode case study

The printing process and parameters were tested to ensure their viability of the proposed methodology. The parameter set of Test 39 (P=400 W, t = 0.3 s, and Q=5 g·min^{-1}) was chosen for printing the DotCode, as it allowed the printing of a more compact code.

The code shown in Fig. 14 was successfully read from both sides of the sample and images of the same quality were obtained despite being located 1.2 mm deep from the ground side and 10 mm from the back plate side. This proved the independence of the X-ray readability from the code location depth, which allows the code to be further away from the surface, with the aim of maintaining its properties. Therefore, the proposed methodology is suited for creating embedded codes without interfering with the surface hardness, wear resistance, biocompatibility and osteo-integrability of the original part.

On the other hand, the dot diameter deviation shown in Fig. 14 illustrate that the X-ray measurements of the dots decrease slightly from the right to the left of the code, the values for the mean diameter value and the standard deviation being 1.378 mm and 0.074 mm respectively. This deviation can be derived from the non-homogenous distribution of the number of particles injected in each dot, or a slight change in the working distance during the printing of the code. Nevertheless, this size variation does not interfere with the readability of the final code.

3.6. Mechanical property testing results

The flexural behaviour was evaluated by means of the 3-point bending tests. Three situations were analysed: 1) Ti6Al4V substrate material, 2) Ti6Al4V substrate with a 1.2 mm DED-LB Ti6Al4V coating, and 3) Ti6Al4V substrate with a 1.2 mm DED-LB Ti6Al4V coating embedding a DotCode section. Their flexural behaviour is represented in Fig. 15.

The material extracted from the Titanium base showed a ductile behaviour and did not fracture during testing, as shown on Fig. 15(a). In comparison, the specimens from coated regions showed a loss in ductility, reaching the breaking point at a 1.52 ± 0.20 mm vertical displacement in the case of the coated samples and 0.39 ± 0.05 mm in the case of coded and coated. Plastic deformation of the material occurred at around 2.4 kN in all the analysed samples, proving that the DED-LB processing did not affect the elastic limit of the material.

Taking the coated samples without WC inclusions as a baseline, the ultimate load of the samples decreases by 21.69 % when introducing the DotCode at 1.2 mm from the surface, as a result of the increased hardness and subsequent loss of ductility of the matrix. The fracture images from Fig. 15(b) and (c) further illustrate the impact of WC particles on the material behaviour. As seen in Fig. 15(a), the samples from coated regions deformed elastically until a load of 2.4 kN and continued plastically deforming until fracture. This deformation is depicted in Fig. 15 (b), where the necking has decreased the width of the sample by 7.9 %. On the other hand, the samples containing WC particles had no plastic deformation before fracture, Fig. 15(c).

The aforementioned results highlight that any DED-LB processing of the part, regardless of WC inclusions, had an effect on the behaviour of the base titanium part. This effect was increased for the samples with WC inclusions, which increased the hardness of the surrounding matrix material and therefore reduced its ductility.

The surface hardness measurements obtained a 38.1 ± 1.1 and 39.4 ± 1.4 HRC mean hardness values for the titanium base material, and the coded and coated surface, respectively. This proves that although the WC inclusions increased the hardness of the matrix locally, the surface properties remained similar to those of the original part, despite the code being located 1.2 mm deep.

4. Summary and conclusions

In the present research a novel subcutaneous coding system was developed and validated for unalterable metallic component identification. The proposed methodology can produce a subcutaneous code, such as a DotCode, invisible from the outside but detectable via X-ray. In the developed methodology two compatible materials of very different densities were paired, Ti6Al4V and WC, employing the laser-based directed energy deposition (DED-LB) process. Moreover, the validity of the system was ensured by printing a demonstrator DotCode with the word “certified” according to the AIM standard. Hereafter the main conclusions obtained from the present research are summarized:

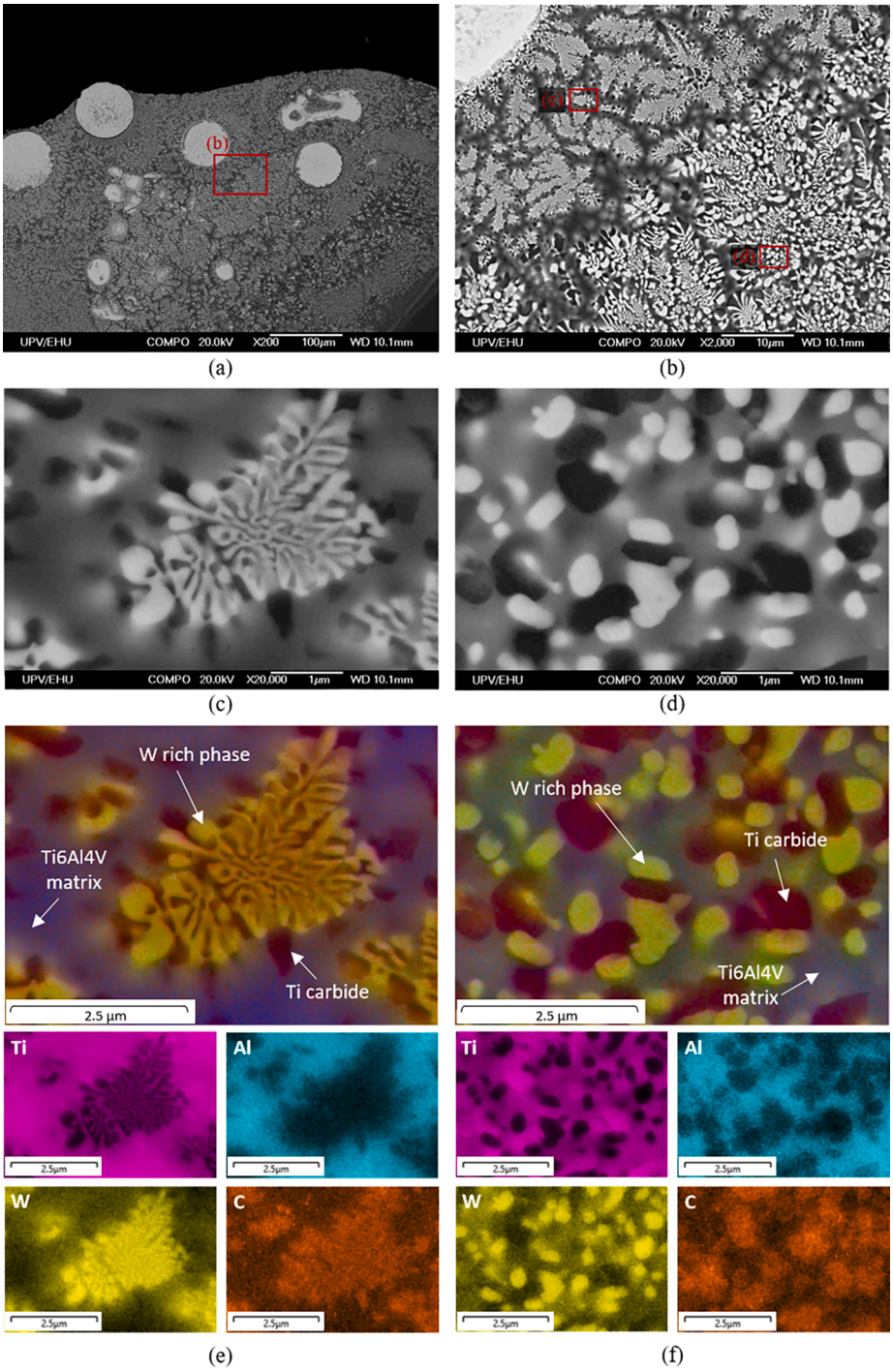

Fig. 12. Microstructural analysis of Test 39. (a) Test 39 cross section where a microstructural change is observed, (b) microstructural change detail with x2,000 magnification, (c) detail on a fine microstructure zone with x20,000 magnification, (d) detail on a coarse microstructure zone with x20,000 magnification, (e) EDS compositional maps of the fine microstructure shown in (c), (f) EDS compositional maps of the coarse microstructure shown in (d).

- The generation of embedded discrete dots through the deposition of MMC has proven to be an effective technique for generating non-visible and unalterable codes for component identification. The embedded code can be read through X-ray inspection without damaging the component.
- The dimensions and readability of the individual dots depended on the employed process parameters: laser power, pulse duration, and WC mass feed rate. According to the parameter analysis, laser power had the most significant impact on the generated dot diameter, followed by the pulse duration. On the contrary, dot readability was mostly dependent on the WC mass feed rate, and values above 4 $g \cdot min^{-1}$ were necessary to obtain readable dots. Computed tomography (CT) also verified these results, by allowing the comparison of high-density regions on each dot.
- The proposed methodology has led to the identification of two optimum process parameter sets for the DotCode printing: a high spatial resolution option (Test 39) for the fabrication of a compact code with smaller (1.5 mm diameter) dots and a higher readability option (Test 45) with improved contrast at the cost of larger (2 mm diameter) dots. The first one is geared towards smaller size parts and

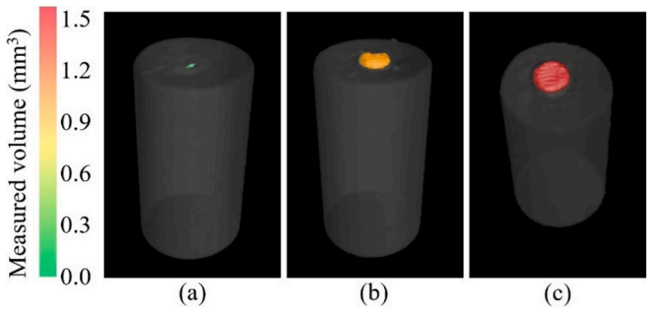

Fig. 13. Computed tomography images and measured volumes. (a) Low contrast reference parameter set test 9. (b) Optimal parameter set for high spatial resolution test 39. (c) Optimal parameter set for high X-ray resolution test 45.

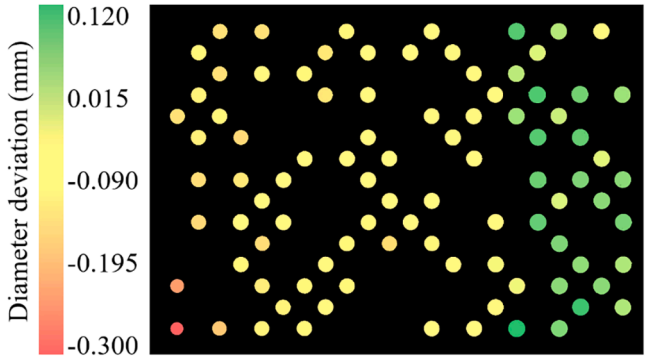

Fig. 14. Final DotCode analysis. Dot size analysis and diameter size deviation on the fabricated code, from a mean diameter value of 1.378 mm and with a standard deviation of 0.074 mm (1STDEV).

the second one for larger parts where readability might be more critical.

- Discrete WC particles were distributed within the melted area and generated a higher density dot. A larger number of embedded particles showed an increase in the formation of (TiW)C solid solution in the matrix, which had a higher density than the Ti6Al4V substrate material.
- The microstructure of the fabricated dots presented no internal defects, such as cracks or internal voids (pores and lack of fusion).
- In the compositional analysis it was concluded that the deposited dot has a higher density not only in the individual locations of the discrete WC particles, but also in the whole region melted by the laser. The underlying reason for this was that within the Ti6Al4V matrix W rich phases were encountered distributed in the whole dot, surrounded by TiC precipitates which nucleate around them.
- A demonstrator was manufactured with the word "certified" codified inside the material. The DotCode was coated via DED-LB, and X-ray imaging ensured that the code depth does not affect its readability. Therefore, the X-ray systems resolution is the only limitation for the total thickness of the coded region. In the present case, clear readings of a 12 mm thick Ti6Al4V plate were obtained. Consequently, the code can be positioned relatively far from the surface, which ensures that the surface properties of the part will not be affected by the embedded code.
- An analysis of the dots composing the code demonstrated that, due to the characteristics of the process the individual dots are not fully identical. Despite this, the DotCode was successfully identified.
- Flexural tests proved that the inclusion of WC particles at 1.2 mm deep reduced the plastic deformation range of the material, resulting in a 21.69 % reduction on maximal load in comparison to coated samples. However, coding process had little impact on the surface

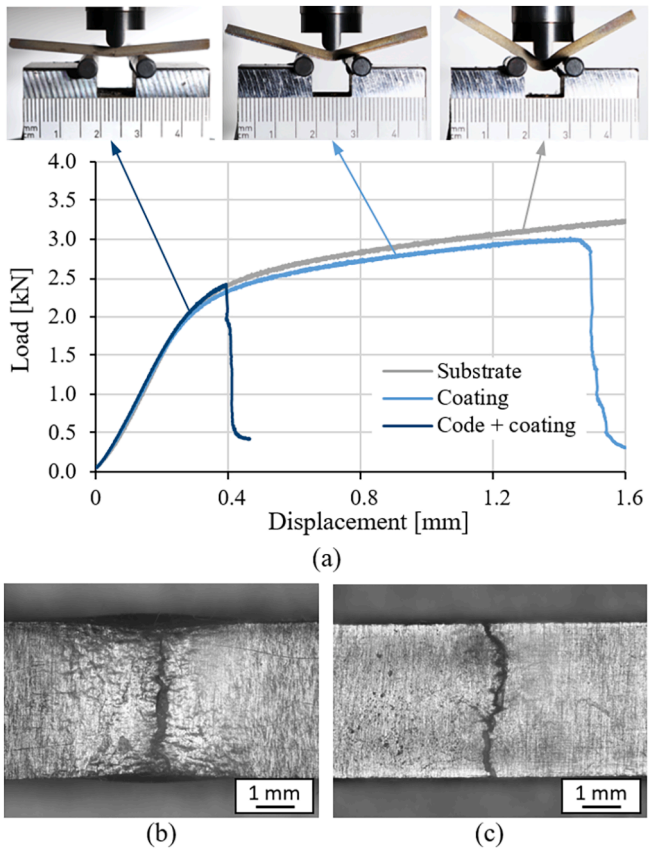

Fig. 15. 3-point bending test results. a) Load vs. displacement data corresponding to 3-point bending tests and fracture images of specimen with b) Ti6Al4V base and Ti6Al4V coating, and c) Ti6Al4V base with WC inclusions and Ti6Al4V coating.

hardness of the part and no differences are encountered in the elastic behaviour of the material.

Although the proposed methodology has provided good results for the analysed geometries, it is clear it also poses some limitations in terms of coded part geometry. As previously mentioned, the X-ray machines maximum voltage and size limit the resolution of the obtained images, as well as the maximum thickness of the coded region of the part. Because of this, the placement of the code inside the part will be dictated by the thickness of the different regions. Additionally, the stress level of the selected region will need to be considered, in order not to interfere with the mechanical behaviour of the coded components.

CRediT authorship contribution statement

Aizpea Urresti: Writing – original draft, Validation, Methodology, Investigation, Formal analysis, Data curation. **Jon Iñaki Arrizubieta:** Writing – original draft, Validation, Methodology, Conceptualization. **Aitzol Lamikiz:** Supervision, Methodology, Funding acquisition. **Ibon Holgado:** Writing – original draft, Validation, Data curation. **Naiara Ortega:** Supervision, Resources.

Declaration of competing interest

The authors declare the following financial interests/personal relationships which may be considered as potential competing interests: Jon Inaki Arrizubieta Arrate reports financial support was provided by Basque Government. Jon Inaki Arrizubieta reports financial support was provided by Spain Ministry of Science and Innovation. Aitzol Lamikiz reports financial support was provided by Basque Government. If there

are other authors, they declare that they have no known competing financial interests or personal relationships that could have appeared to influence the work reported in this paper.

Data availability

Data will be made available on request.

Acknowledgements

This work was supported by the ELKARTEK program of the Dept. of Economic Development, Sustainability and Environment of the Basque Government [grants KK-2022/00080 and KK-2023/00096], and by the MCIN/AEI/10.13039/501100011033/ and ERDF A way of making Europe [grant PID2022-141946OB-C21].

Appendix 1

Conditions and geometrical results for the single pulse tests, where P, t, and Q represent the laser power, pulse duration and powder feed rate, respectively. D_{real} stands for the diameter measurements by optical microscope, while the diameter of the dots read by X-ray imagining are in $D_{X\text{-}ray}$.

No.	P (W)	t (s)	Q (g·min^{-1})	D_{real} (mm)	$D_{X\text{-}ray}$ (mm)
1	400	0.1	1	1.380	0.000
2	400	0.2	1	1.475	0.513
3	400	0.3	1	1.540	0.998
4	500	0.1	1	1.660	0.112
5	500	0.2	1	1.760	0.855
6	500	0.3	1	1.830	1.046
7	600	0.1	1	1.905	0.000
8	600	0.2	1	2.025	0.963
9	600	0.3	1	2.140	1.353
10	400	0.1	2	1.415	0.671
11	400	0.2	2	1.475	1.102
12	400	0.3	2	1.535	1.177
13	500	0.1	2	1.660	0.402
14	500	0.2	2	1.765	1.249
15	500	0.3	2	1.785	1.496
16	600	0.1	2	1.910	1.209
17	600	0.2	2	2.005	1.557
18	600	0.3	2	2.060	1.726
19	400	0.1	3	1.380	0.796
20	400	0.2	3	1.480	1.138
21	400	0.3	3	1.570	1.347
22	500	0.1	3	1.660	1.197
23	500	0.2	3	1.720	1.393
24	500	0.3	3	1.785	1.539
25	600	0.1	3	1.885	1.200
26	600	0.2	3	1.985	1.638
27	600	0.3	3	2.005	1.800
28	400	0.1	4	1.405	1.038
29	400	0.2	4	1.455	1.237
30	400	0.3	4	1.570	1.433
31	500	0.1	4	1.645	1.242
32	500	0.2	4	1.755	1.445
33	500	0.3	4	1.805	1.733
34	600	0.1	4	1.855	1.528
35	600	0.2	4	1.915	1.724
36	600	0.3	4	2.025	1.911
37	400	0.1	5	1.360	1.107
38	400	0.2	5	1.530	1.449
39	400	0.3	5	1.595	1.576
40	500	0.1	5	1.600	1.438
41	500	0.2	5	1.710	1.648
42	500	0.3	5	1.865	1.856
43	600	0.1	5	1.850	1.555
44	600	0.2	5	1.960	1.877
45	600	0.3	5	2.055	2.013

Appendix A. Supplementary data

Supplementary data to this article can be found online at https://doi.org/10.1016/j.matdes.2024.113218.

References

[1] Europol, n.d. Counterfeiting and Product Piracy. https://www.europol.europa.eu/crime-areas-and-statistics/crime-areas/intellectual-property-crime/counterfeiting-and-product-piracy.

[2] R. Schuitemaker, X. Xu, Product traceability in manufacturing: a technical review, Procedia CIRP 93 (2020) 700–705, https://doi.org/10.1016/J.PROCIR.2020.04.078.

[3] C. Velotti, A. Astarita, C. Leone, S. Genna, F.M.C. Minutolo, A. Squillace, Laser marking of titanium coating for aerospace applications, Procedia CIRP 41 (2016) 975–980, https://doi.org/10.1016/J.PROCIR.2016.01.006.
[4] K. Ludasi, et al., Anti-counterfeiting protection, personalized medicines – development of 2D identification methods using laser technology, Int. J. Pharm. 605 (2021) 120793, https://doi.org/10.1016/J.IJPHARM.2021.120793.
[5] S. Teutoburg-Weiss, F. Sonntag, K. Günther, A.F. Lasagni, Multiple method micromachining laser platform for fabricating anti-counterfeit elements with multiple-scaled features, Opt. Laser Technol. 115 (2019) 465–476, https://doi.org/10.1016/J.OPTLASTEC.2019.02.044.
[6] A.O. Larin, et al., Luminescent erbium-doped silicon thin films for advanced anti-counterfeit labels, Adv. Mater. 33 (2021) 2005886, https://doi.org/10.1002/adma.202005886.
[7] A. Speidel, I. Bisterov, A.T. Clare, Direct writing unclonable watermarks with an electrochemical jet, Adv. Funct. Mater. 32 (2022) 2208116, https://doi.org/10.1002/adfm.202208116.
[8] F. Chen, G. Mac, N. Gupta, Security features embedded in computer aided design (CAD) solid models for additive manufacturing, Mater. Des. 128 (2017) 182–194, https://doi.org/10.1016/J.MATDES.2017.04.078.
[9] N. Raeker-Jordan, J. Chung, Z. Kong, C. Williams, Ensuring additive manufacturing quality and cyber–physical security via side-channel measurements and transmissions, J. Manuf. Syst. 73 (2024) 275–286, https://doi.org/10.1016/j.jmsy.2024.02.005.
[10] H.T. Maia, D. Li, Y. Yang, C. Zheng, LayerCode: optical barcodes for 3D printed shapes, ACM Trans. Graph. 38 (2019), https://doi.org/10.1145/3306346.3322960.
[11] C. Wei, Z. Sun, Y. Huang, L. Li, Embedding anti-counterfeiting features in metallic components via multiple material additive manufacturing, Addit. Manuf. 24 (2018) 1–12, https://doi.org/10.1016/J.ADDMA.2018.09.003.
[12] F. Chen, J. Zabalza, P. Murray, S. Marshall, J. Yu, N. Gupta, Embedded product authentication codes in additive manufactured parts: imaging and image processing for improved scan ability, Addit. Manuf. 35 (2020) 101319, https://doi.org/10.1016/J.ADDMA.2020.101319.
[13] D. Eisenbarth, P. Stoll, C. Klahn, T.B. Heinis, M. Meboldt, K. Wegener, Unique coding for authentication and anti-counterfeiting by controlled and random process variation in L-PBF and L-DED, Addit. Manuf. 35 (2020) 101298, https://doi.org/10.1016/j.addma.2020.101298.
[14] T. Schmitz, et al., Embedded QR code for part authentication in additive friction stir deposition, Manuf. Lett. 35 (2023) 16–19, https://doi.org/10.1016/j.mfglet.2022.11.003.
[15] M. Ostolaza, J.I. Arrizubieta, A. Queguineur, K. Valtonen, A. Lamikiz, I. Flores Ituarte, Influence of process parameters on the particle–matrix interaction of WC-Co metal matrix composites produced by laser-directed energy deposition, Mater. Des. 223 (2022) 111172, https://doi.org/10.1016/J.MATDES.2022.111172.
[16] L. Liu, et al., Laser additive manufacturing of a 316L/CuSn10 multimaterial coaxial nozzle to alleviate spattering adhesion and burning effect in directed energy deposition, J. Manuf. Process. 82 (2022) 51–63, https://doi.org/10.1016/J.JMAPRO.2022.07.038.
[17] D. Salas, D. Ebeperi, M. Elverud, R. Arróyave, R.J. Malak, I. Karaman, Embedding hidden information in additively manufactured metals via magnetic property grading for traceability, Addit. Manuf. 60 (2022) 103261, https://doi.org/10.1016/J.ADDMA.2022.103261.
[18] C. Zhang, D. Zou, M. Mazur, J.P.T. Mo, G. Li, S. Ding, The state of the art in machining additively manufactured titanium alloy Ti-6Al-4V, Materials (basel) 16 (2023), https://doi.org/10.3390/ma16072583.
[19] X. Yang, L. Wang, Z. Gao, Q. Wang, M. Du, X. Zhan, WC distribution, microstructure evolution mechanism and microhardness of a developed Ti-6Al-4V/WC MMC coating fabricated by laser cladding, Opt. Laser Technol. 153 (2022) 108232, https://doi.org/10.1016/j.optlastec.2022.108232.
[20] O. Oyelola, P. Crawforth, R. M'Saoubi, A.T. Clare, Machining of functionally graded Ti6Al4V/ WC produced by directed energy deposition, Addit. Manuf. 24 (2018) 20–29, https://doi.org/10.1016/J.ADDMA.2018.09.007.